Vortex with fourfold defect lines in a simple model of self-propelled particles

Hamid Seyed-Allaei and Mohammad Reza Ejtehadi[*]

Department of Physics, Sharif University of Technology, P.O. Box 11155-9161, Tehran, Iran
(Received 9 September 2015; revised manuscript received 12 December 2015; published 8 March 2016)

We study the formation of a vortex with fourfold symmetry in a minimal model of self-propelled particles, confined inside a squared box, using computer simulations and also theoretical analysis. In addition to the vortex pattern, we observe five other regimes in the system: a homogeneous gaseous phase, band structures, moving clumps, moving clusters, and vibrating rings. All six regimes emerge from controlling the strength of noise and from the contribution of repulsion and alignment interactions. We study the shape of the vortex and its symmetry in detail. The pattern shows exponential defect lines where incoming and outgoing flows of particles collide. We show that alignment and repulsion interactions between particles are necessary to form such patterns. We derive hydrodynamical equations with an introduction of the "small deviation" technique to describe the vortex phase. The method is applicable to other systems as well. Finally, we compare the theory with the results of both computer simulations and an experiment using Quincke rotors. A good agreement between the three is observed.

I. INTRODUCTION

It is likely that most people have observed the fascinating movement patterns of flocks of birds [1–3] or schools of fish [4,5]. Similar structures are widely seen in many places, ranging from the size of the human body [6] down to nanometer scales [7,8], and such structures can include either living individuals [9,10] or nonliving ones [11,12]. The common feature among all of these diverse systems is activity among the individuals, thus these systems are referred to as "active matter." Active matter, because of the consumption and injection of energy, is always out of equilibrium, and in recent years it has attracted a great deal of attention [13,14]. In one of the first studies on active matter, collective patterns from basic local interactions were produced [15]. After that, phenomenological theories as well as microscopic descriptions were established to identify the characteristics and features of active matter [16–19]. In addition, more complex collective patterns were observed with the introduction of new models [20–22], and they helped to improve knowledge of the phase transitions and behavior of active matter [23–27].

Vortices are one of the most interesting patterns observed in active matter. Some biological examples of vortex formation include swirling daphnia around a light shaft [28], bacteria rotating in droplets of *bacillus subtilis* morphotype, which grow on an agar substrate [9], and vortices formed by the movement of actin filaments on a surface coated with heavy meromyosin [8]. . There are also nonbiological examples of vortex formation, e.g., vertically vibrating granular rods [29], anisotropic rods in a container [30], and micrometer-sized insulator spheres that are more commonly known as Quincke rotors [31]. In addition to stable vortex patterns, the dissipation of vortices (e.g., in a turbulent phase) is observed in colonies of bacteria [32,33]. Many studies have been performed in an effort to understand the nature and characteristics of vortex formation. For example, a model of self-propelled particles that repel each other at close distances and attract when far apart creates a giant vortex [34]. Another example is the case

of particles with intrinsic curvature in their motion, such as microtubules moving on a surface coated with myosines [35]. More sophisticated models take into account chemotaxis and the proliferation of bacteria to explain their swirling motion [9]. It is also possible to have a vortex array in a system [36,37] acquiring self-propelled particles with alignment and antialignment interactions with respect to distance [36] or time-correlated noise [37].

In an experimental study of Quincke rotors [31], the particles and their interactions produced a complex vortex inside a square box, and the vortex exhibited fourfold symmetry. This fourfold shape occurs in conjunction with an effect that we call hereafter "suppressed spreading." In suppressed spreading, particles that are bounced back from a corner tend to spread over all available directions, but because of the flow of the other particles and the collisions, the spreading of the outgoing flow is suppressed and is limited to a smaller angle. Suppressed spreading is visible as a curved boundary where the direction and density of the particles change spontaneously, and we call this boundary the "defect line."

In this study, we were inspired by experimental vortex formations [7,31] to explore a vortex pattern of self-propelled particles confined in a geometry. Similar studies were performed by simulating active granular particles with inelastic interactions confined in a square box [38,39]. However, those studies were limited in size, and because of their inelastic interaction they could not describe the complex structures and density jump lines of the Quincke rotors observed in the experiments [31].

We introduce a minimal model and find the key elements required to have a vortex with the symmetry of confining geometry (Sec. II). The model is a simple generalization of the continuous Vicsek model [9] with alignment and repulsion interactions. Both interactions have a physical interpretation, and they were derived theoretically in Ref. [31]. The important role of repulsion in vortex formation was revealed recently [40]. Next, we derive continuum hydrodynamic equations in the limits of high and low noise in order to compare the solutions with the particle model and the experimental results (Sec. III). Finally, we present the results of our simulations, and we discuss the patterns and their characteristics (Sec. IV).

_____
[*]ejtehadi@sharif.edu

II. MODEL

We consider two-dimensional self-propelled particles with the same constant speed v_0. The angle of velocity with the x axis is θ, and the direction of motion for each particle is toward $\hat{v}_\theta$. The direction of each particle is changed by torque. This torque originates from particle-particle and wall-particle interactions. For the dynamics of the particles, we consider

$$\dot{\vec{r}}_i = v_0 \hat{v}_{\theta_i}, \qquad (1)$$

$$\zeta \dot{\theta}_i = \tau_i^p + \tau_i^w + \epsilon \eta_i(t), \qquad (2)$$

where $\vec{r}_i$ is the position of the ith particle, and $\hat{v}_{\theta_i}$ is a unit vector along the swimming direction of the particle with angle θ_i [$\hat{v}_\theta = \cos(\theta_i)\hat{e}_x + \sin(\theta_i)\hat{e}_y$]. Equation (2) is an overdamped Langevin equation over θ_i. ζ is the friction coefficient, τ_i^p and τ_i^w are the torques acting on the particle i from the other particles and the walls, respectively. We added a noise term $\epsilon \eta_i(t)$ that represents the stochastic behavior of self-propelled particles and their environment, where $\eta_i(t)$ is Gaussian uncorrelated white noise with $\langle \eta_i(t) \rangle = 0$ and $\langle \eta_i(t)\eta_i(t') \rangle = \delta(t - t')$, and ϵ is the noise amplitude. Without loss of generality, the value of ζ is set to 1 in this paper because one can divide both sides of Eq. (2) by the friction coefficient and redefine the noise and interaction strength.

The particle-particle interaction is a combination of alignment and repulsion. Alignment means particles rotate to make their moving directions parallel to each other, and repulsion means that particles rotate to move away from each other (Fig. 1). The alignment and repulsion interactions that are close to Quincke rotors interactions [31] give

$$\tau_{ji} = \frac{g_p}{\pi} A(r_{ji})\big[(1-\alpha)\sin(\theta_j - \theta_i) + \alpha(\hat{r}_{ji} \wedge \hat{v}_{\theta_i}) \cdot \hat{e}_z\big]. \quad (3)$$
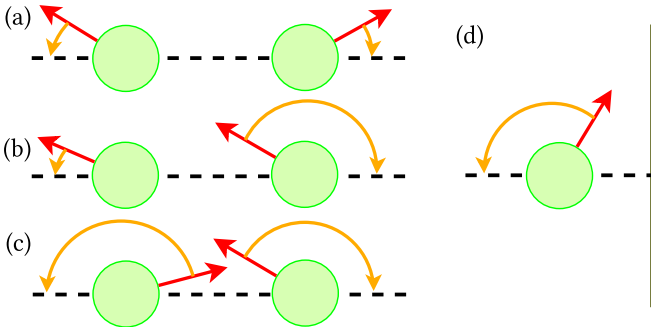

FIG. 1. Repulsive torque between two particles in Eq. (3) (a)–(c) and between a particle and a wall in Eq. (5) (d). Each particle is represented by a green (light gray) disk. The straight red (light gray) arrow shows the direction of the particle. The arced orange (dark gray) arrow shows the direction of rotation, the end of this arrow is the particle's final direction, and its length has no relation to the magnitude of the torque. The thick vertical line is a wall. The dashed lines in (a)–(c) represent the interdistance line between two colliding particles, and in (d) the dashed line is perpendicular to the wall. In (a) the particles are escaping and the torque intensifies this escape. In (b) the particles are moving together and the torque causes them to move away. In (c) the particles are moving toward one another and the torque prevents them from reaching each other. In (d) the particle is moving toward the wall.

The first term on the right-hand side (RHS) is aligning and the second term is repulsive torque. $\vec{r}_{ji}$ is the distance vector from particle j to i, g_p is the strength of particle-particle interaction, and $A(r_{ji})$ is a function of interparticle distance. $0 \leqslant \alpha \leqslant 1$ controls the relative contribution of repulsion and alignment terms, i.e., $\alpha = 0$ corresponds to the original continuous Vicsek model, and $\alpha = 1$ corresponds to a fully repulsive particle system. It is also interesting to see the result of negative α that is a combination of alignment and attraction. The $\wedge$ sign between vectors indicates a vector product. The model is two-dimensional, but for a compact presentation we use a dot product of a unit vector along the z axis, $\hat{e}_z$, with the outer product of two-dimensional (2D) vectors as a scalar value.

Figure 1 shows a schematic presentation of interaction terms. As one can see, repulsion reverses the particles from their interdistance direction.

For simplicity, we restrict ourselves here to the case of constant α, and we consider a Heaviside step function for A,

$$A(r_{ji}) = \Theta(R - r_{ji}), \qquad (4)$$

where R indicates the range of interaction between the particles. We set our length unit such that $R = 1$.

Very similar to the repulsive interaction between particles, if we label a wall by w, the applied torque by the wall w on a particle i is given by

$$\tau_{wi} = \frac{g_w}{\pi r_{wi}} A(r_{wi})\big[(\hat{n}_w \wedge \hat{v}_{\theta_i}) \cdot \hat{e}_z\big], \qquad (5)$$

where $\hat{n}_w$ is the unit normal vector of the wall, r_{wi} is the distance of the particle from the wall, and g_w is the strength of the particle-wall interaction. The factor $1/r_{wi}$ guarantees that the particles never pass the wall.

One should note that in contrast to the alignment torque, the repulsion torque will not conserve the total angular momentum. In models with spontaneous vortex formation, a generating source of angular momentum is necessary.

In the next section, we will use this microscopic model to obtain the hydrodynamic equations of the system.

III. HYDRODYNAMIC EQUATIONS

Let $f(\theta,\vec{r})$ be the density of particles at point $\vec{r}$ with angle θ, and let $P(\theta,\vec{r})$ be the orientational probability distribution of particles at point $\vec{r}$. We can simply write the density of particles in terms of $f(\theta,\vec{r})$, that is,

$$\rho(\vec{r}) = \int_0^{2\pi} f(\theta,\vec{r})d\theta, \qquad (6)$$

and we write a relation between f, P, and ρ,

$$f(\theta,\vec{r}) = \rho(\vec{r})P(\theta,\vec{r}). \qquad (7)$$

In our system, important quantities are the polarization vector,

$$\vec{\mathcal{P}}(\vec{r}) = \langle \hat{v}_\theta \rangle = \int_0^{2\pi} \hat{v}_\theta P(\theta,\vec{r})d\theta, \qquad (8)$$

and the momentum flux,

$$\vec{W}(\vec{r}) = \rho\langle \hat{v}_\theta \rangle = \int_0^{2\pi} \hat{v}_\theta f(\theta,\vec{r})d\theta. \qquad (9)$$

We are going to derive a hydrodynamic equation for continuous quantities ρ, $\vec{W}$, and $\vec{\mathcal{P}}$. The starting point is to use the Boltzmann approximation to derive the Fokker-Planck equation, which has the form

$$\frac{\partial f(\theta, \vec{r})}{\partial t} = -\frac{\partial}{\partial \theta}(f V_{\text{drift}}) + D_r \frac{\partial^2 f}{\partial \theta^2} - v_0 \hat{v}_\theta \cdot \vec{\nabla} f. \quad (10)$$

Here V_{drift} represents the Fokker-Planck drift velocity, and $D_r = \epsilon^2/2$ is the rotational diffusion of particles. The drift velocity originates from alignment and repulsion interactions, and it is given in Appendix A [Eq. (A1)]. The second term on the RHS of Eq. (10) denotes rotational diffusion, and the third term denotes advection of the particles. The Fokker-Planck equation depends on $f(\theta, \vec{r})$, a field with two variables, and it is complicated to work with. We need a simpler equation over ρ, $\vec{\mathcal{P}}$, and $\vec{W}$. One of the equations is the continuity equation, and it can be obtained by integrating both sides of Eq. (10) over θ from 0 to 2π and using the definition of Eq. (9):

$$\frac{\partial \rho}{\partial t} + v_0 \vec{\nabla} \cdot \vec{W} = 0. \quad (11)$$

The other equation is more subtle and needs some approximation. There are two different approximations. One is done in high noise with condition $D_r \gg D_{lb}$, where $D_{lb} = 0.16$, for parameters $v_0 = 1$, $g_p = 2$, and $\alpha = 0.5$. The high noise approximation is commonly used in active matter problems [20,41]. We present the details of this method and its validity condition in Appendix A. The other approximation, however, is rather new and is valid in low noise with condition $D_r \ll D_{ub}$, where $D_{ub} = (1 - \alpha)g_p\rho$. We call the new method in low noise the "small deviation" method, and it is presented with details in Appendix B.

A. High-noise limit

We can summarize the high-noise hydrodynamic equations (see Appendix A) in the following form:

$$\dot{\vec{W}} = \vec{W}_f + \vec{W}_\nabla, \quad (12)$$

where $\vec{W}_f$ is

$$\vec{W}_f = \left[\frac{(1-\alpha)\rho g_p}{2} - D_r - \frac{(1-\alpha)^2 g_p^2 W^2}{8 D_r} \right] \vec{W}, \quad (13)$$

which causes spontaneous polarization, and it usually appears in active matter hydrodynamic equations [16,41–43]. $\vec{W}_\nabla$ contains the terms that have spatial derivatives. The exact form of $\vec{W}_\nabla$ is given in Appendix A [Eq. (A3)].

In the homogeneous solution of Eq. (12), all spatial derivatives are zero, i.e., $\vec{W}_\nabla = 0$. Therefore, $\vec{W}_f$ is the remaining term that drives the momentum flux. In a system with initial density ρ_0, the factor behind $\vec{W}$ on the RHS of Eq. (13) changes sign at rotational diffusion $D_c = \epsilon_c^2/2$ corresponding to noise strength $\epsilon_c = \sqrt{(1-\alpha)g_p\rho_0}$. This change of sign is at the point of the nonpolar ($\vec{W} = \vec{0}$) to polar transition. The nonpolar to polar transition is important for confined particles because as simulations show, once the system goes to a polar state near the transition noise, particles start to rotate.

To find the inhomogeneous solution of Eq. (12), we can numerically integrate Eqs. (12) and (11). We set the parameters
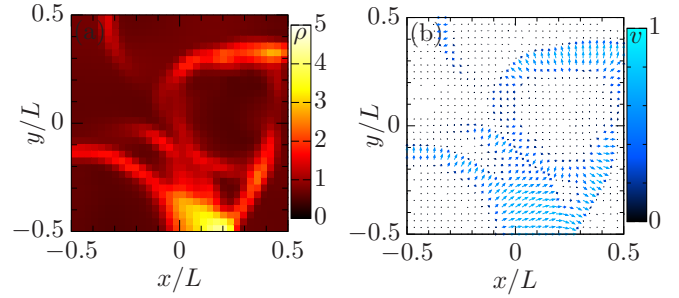

FIG. 2. Results of the continuum model [Eq. (12)] before the occurrence of divergence with initial density $\rho_0 = 1$, alignment interaction $g_p = 2$, repulsion factor $\alpha = 0.5$, and noise $D_r = 0.59$ ($\epsilon = 1.08$) in a box of size $L = 120R$. (a) Density profile. (b) Velocity field; the lengths of the arrows are proportional to the magnitude. Both images correspond to the same moment, and their grid size is 32 by 32.

$g_p = 2$, $\alpha = 0.5$, $\rho_0 = 1$, and the box size $L = 120R$. These parameters give us $D_c = 0.5$. The answer with $D_r \geqslant 0.6$ is nonpolar and homogeneous. Lowering the rotational diffusion creates instability in the system, and we cannot observe vortex formation. But interestingly, we can observe some stripes forming and propagating in the box at the initial stage of computation before divergence occurs (Fig. 2). The instability is a consequence of our criteria for the validity of high-noise hydrodynamic equations ($D_c \gg D_{lb}$). The inability to capture the behavior of the system in the vortex regime motivated us to introduce the small deviation method in the low-noise limit.

B. Low-noise limit

The small deviation method, described in Appendix B, leads us to an equation for $\dot{\vec{\mathcal{P}}}$. Like high-noise equations, we split the evolution of $\vec{\mathcal{P}}$ into derivative $\vec{\mathcal{P}}_\nabla$ and nonderivative $\vec{\mathcal{P}}_f$ terms,

$$\dot{\vec{\mathcal{P}}} = \vec{\mathcal{P}}_f + \vec{\mathcal{P}}_\nabla, \quad (14)$$

with

$$\vec{\mathcal{P}}_f = \vec{\mathcal{P}}[2(1-\alpha)\rho g_p(1-\mathcal{P}) - D_r], \quad (15)$$

and $\vec{\mathcal{P}}_\nabla$ is described in Appendix B [Eq. (B4)].

By examining the homogeneous case of Eq. (14), we see that the transition point of the nonpolar to polar state is $\epsilon_c' = 2\sqrt{(1-\alpha)g_p\rho_0} = 2\epsilon_c$. Therefore, we see that the small deviation approximation is not successful in determining the phase transition. However, since this method uses the assumption of low noise, it must predict well the behavior of the system deep in the ordered state where we have the vortex phase.

It is clear that solving Eq. (14) together with the continuity equation [Eq. (11)] in squared geometry is complicated, therefore we restrict our calculation to a circular box where the scalar variables depend only on the radial component r. We also neglect second-order derivatives that are related to shorter changes of the fields. Even with these assumptions, the presence of a nonhomogeneous steady state is not obvious, and we need to write everything up to the first order of D_r/D_{ub}. With all these simplifications, one

finds that the continuity equation implies that polarization is toward the polar coordinate unit vector $\hat{\phi}$, and the density satisfies the following relation:

$$\rho(r) + \frac{D_r}{(1-\alpha)g_p} \ln(\rho) = c_\rho \ln\left(\frac{r}{r_0}\right), \qquad (16)$$

where $c_\rho = 3v_0/\alpha g_p$ is a factor, and r_0 is a length scale related to the initial density of particles. We can see that at distances shorter than r_0, the density acquires very small values. Similar results with a logarithmic dependence of density are obtained using the Quincke rotors [40]. If the system has no noise ($D_r = 0$), the RHS of Eq. (16) is negative for $r < r_0$, which corresponds to zero density in the center. In fact, no particle reaches the center in a noiseless system, but when turning on the noise, some particles could reach the center with a small chance. Equation (16) describes very well the simulation results (see Figs. 4 and 5 in Sec. IV).

Integrating both sides of Eq. (16) for $D_r = 0$ over the box, one obtains the total number of particles on the left-hand side (LHS) and an expression on the RHS. Replacing the total number of particles with $\rho_0 \pi R_{\text{box}}^2$, one obtains a relation between ρ_0 and r_0,

$$\rho_0 = \frac{3v_0}{2\alpha g_p}\left[\frac{r_0^2}{R_{\text{box}}^2} - 1 - 2\ln\left(\frac{r_0}{R_{\text{box}}}\right)\right], \qquad (17)$$

where R_{box} is the radius of the circular box. Equation (17) shows that r_0 decreases either by increasing ρ_0 or αg_p, both causing stronger steric repulsions. Although our dynamics is not Newtonian, we see the dependence of r_0/R_{box} on v_0. Because this effect has a mixture of particles with different velocities, it can separate fast and slow particles. We will discuss this effect and the phase separation of slow and fast particles in future work. It is worth mentioning that a mixture of fast and slow particles could be prepared experimentally by using different sizes of Quincke rotors.

C. Numerical method in the computation of the noiseless system

We integrate numerically the hydrodynamic equations of the low-noise limit [Eqs. (14) and (11)] inside a square box when $D_r = 0$ ($\mathcal{P} = 1$). For numerical stability, we rewrite the equations in terms of $\vec{W}$. The integration gives us the value of the fields ρ and $\vec{W}$, but one should keep in mind that in the hydrodynamic limit and its governing equations, there is no guarantee of having positive values for the density everywhere. Physically this is unacceptable but it may occur mathematically, and in the result some points might have a negative density that is unavoidable. Negative densities make the enumeration unstable, and we need to add a $K\nabla^2\rho$ ($K = 0.2$) term to the continuity equation to avoid large negative density values. This extra term does not drastically change the underlying physics of the model, and this technique was used in the literature before [20].

The integration is done using the pseudospectral method, semi-implicit time stepping, and antialiasing (2/3 rule) techniques [44,45]. Using these techniques alone is not enough to achieve stability. We must set $v_0 = 0.005$ at the initial stage of integration and slowly increase the speed up to the highest stable value, which is $v_0 = 0.3$. We set $\alpha = 0.5$ and $g_p = 2$ to compare our result with the particle model. A circular rotating
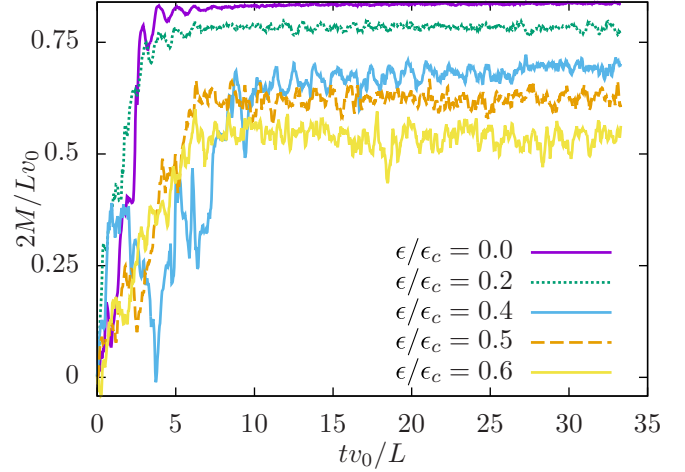

FIG. 3. Angular momentum per particle in time for various noise values. Since we have an isotropic initial condition, at the beginning $M = 0$; after the system evolves, however, the value of M approaches a steady value.

pattern with homogeneous density for the initial condition is necessary to achieve stability. With use of the image method, we apply the slip boundary condition. In other words, we replicate our system on the sides by reflecting $\vec{W}$ to justify the slip boundary condition.

Now we have the right theoretical tools to compare our simulation results. In the next section, we will provide the method and the results of simulations based on the microscopic model to compare with the theory.

IV. SIMULATION

To simulate our model, we used an integration technique (the Ito method [46]) with time steps $dt = 5 \times 10^{-4}$. We set $g_p = 2, g_w = 40$. The speed of the particles is set equal to 1 ($v_0 = 1$) unless otherwise stated. The control parameters in the simulations are the strength of noise ϵ, the repulsion strength α, and the initial density ρ_0. We always put N particles inside a square box with four surrounding walls of size L, except in Sec. IV A, where we use a circular box. The simulation box must be large enough to capture all aspects of a self-propelled system. This limit originates from band structures [47–49] that have typical length scale of v_0/ϵ_c^2. Then for given parameters, one finds the condition $L \gg v_0/\epsilon_c \sim 4$. We initially position particles homogeneously in a triangular lattice with a uniformly random direction of motion. To see the equilibration process of the system, we define the angular momentum per particle,

$$M = \frac{1}{N}\left|\sum_i^N v_0 \vec{r}_i \wedge \hat{v}_{\theta_i}\right|, \qquad (18)$$

and we plot it versus time. Figure 3 shows the evolution of M. We see that after some time, M approaches a steady value. We can sample the system after this time.
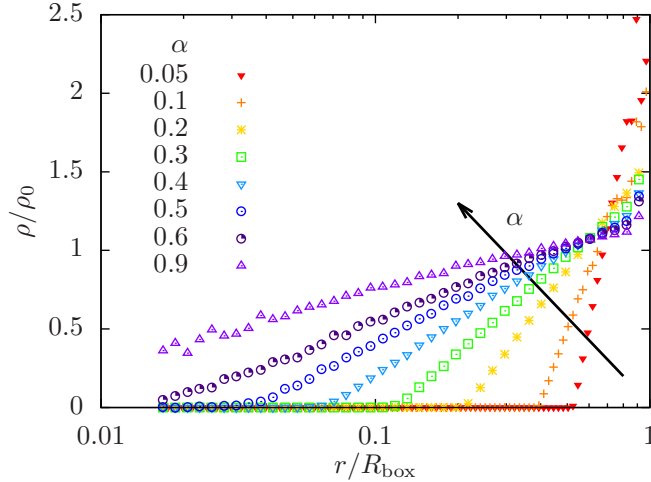
FIG. 4. Density of particles $\rho(r)$ as a function of radial distance r for a noiseless system in a circular box with radius $R_{\text{box}} = 60R$ and initial density $\rho_0 = 8$. Labels show different values of α. One can see that the density increases logarithmically with r [Eq. (16)].

A. Circular box

First we use a circular boundary to compare with the solutions of our theoretical Eqs. (16) and (17). Figure 4 shows the particle density as a function of radial coordinate r for the noiseless microscopic model in a circular box with radius $R_{\text{box}} = 60R$ and initial density $\rho_0 = 8$. The figure shows the results for different values of α. The density is increasing logarithmically with r, and by increasing α a reduction in the slopes and the size of the empty region in the center is visible. Equation (16) predicts exactly the same behavior. For a more precise comparison, we also plot the values of c_ρ and r_0 versus α for given density values $\rho_0 = 1, 2, 4, 8$ in Fig. 5. The dashed lines in Fig. 5 show Eqs. (16) and (17) for each given density. We observe good agreement between theory and simulation, especially for higher densities. This is because at high density, the Boltzmann approximation to derive Eq. (10) and the small deviation approximation are more accurate.

B. Different observed regimes

In simulations of the system with different ϵ and α values, we observed six different regimes: homogeneous gaseous, band structures, moving clumps, moving clusters, vibrating rings, and vortex (see the movies in the Supplemental Material [50]). At a given value of $\alpha = 0.5$, and by decreasing the noise, the homogeneous gaseous phase, the band structures, and the vortex pattern are observed (see Fig. 6). Starting from a very high noise, the system is in a gaseous phase [Fig. 6(a)]. By decreasing the noise strength, the density becomes inhomogeneous, and particles form traveling curved stripes that are due to the reflections from the walls and the corners [Fig. 6(b)]. By further reducing the noise, particles start to rotate in the box, as shown in Fig. 6(c). The direction of rotation is random and depends implicitly on the initial positions and the string of random number samples. In rotation [Fig. 6(c)], one can easily recognize suppressed spreading and the presence of defect lines. The same pattern has been
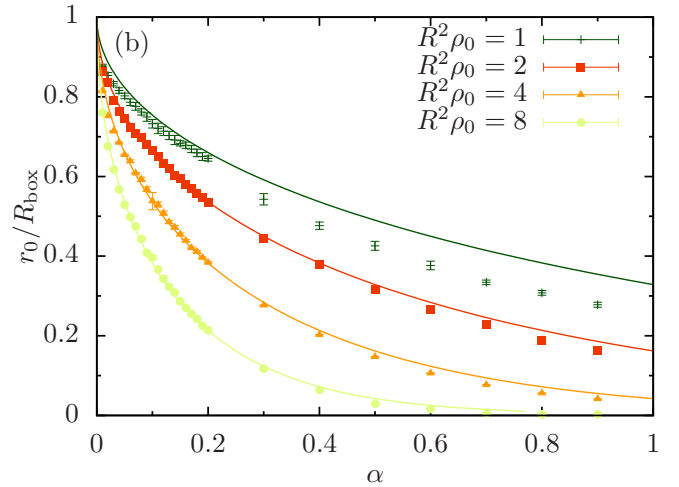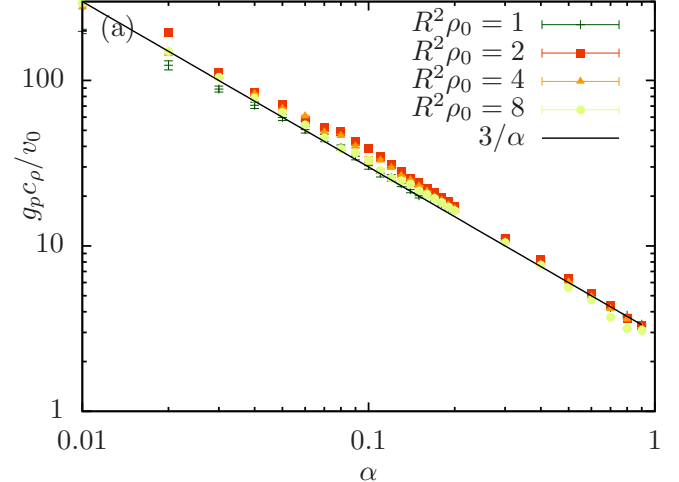

FIG. 5. Comparison of simulations (points with error bars) with theoretical Eqs. (16) and (17) (solid curves) of a circular box with radius $R_{\text{box}} = 60R$ and different initial densities. (a) The plot shows the coefficient c_ρ of Eq. (16) as a function of α. (b) The plot shows r_0/R_{box} as a function of α with different ρ_0 [Eq. (17)].

observed experimentally in the suspension of Quincke rotors [31].

Moving clumps, moving clusters, and vibrating rings can be observed by changing the ratio of repulsion to alignment (Fig. 7). Toward that end, we set $\epsilon = 0.1$ and change α. If we have no alignment ($\alpha = 1$) we obtain a gaseous homogeneous state again, but particles in this homogeneous state have a more robust ballistic motion in comparison to the homogeneous state observed in high noise. A slight decrease in α could lead to the formation of a vortex. Even for very small α we can see rotation, e.g., Fig. 7(a) shows the rotation for $\alpha = 0.01$. Since the repulsion between particles is not strong, they form dense bunches near the walls with a large empty space in the center in such a way that almost all the particles walk on the walls. Upon increasing the repulsion, more space is covered by the particles. By turning off the repulsion completely, particles form very high density clumps that bounce off the walls [Fig. 7(b)]. Clump formation is not observed in the periodic boundary condition because the particles do not meet each other as frequently as confined particles. The shape of the
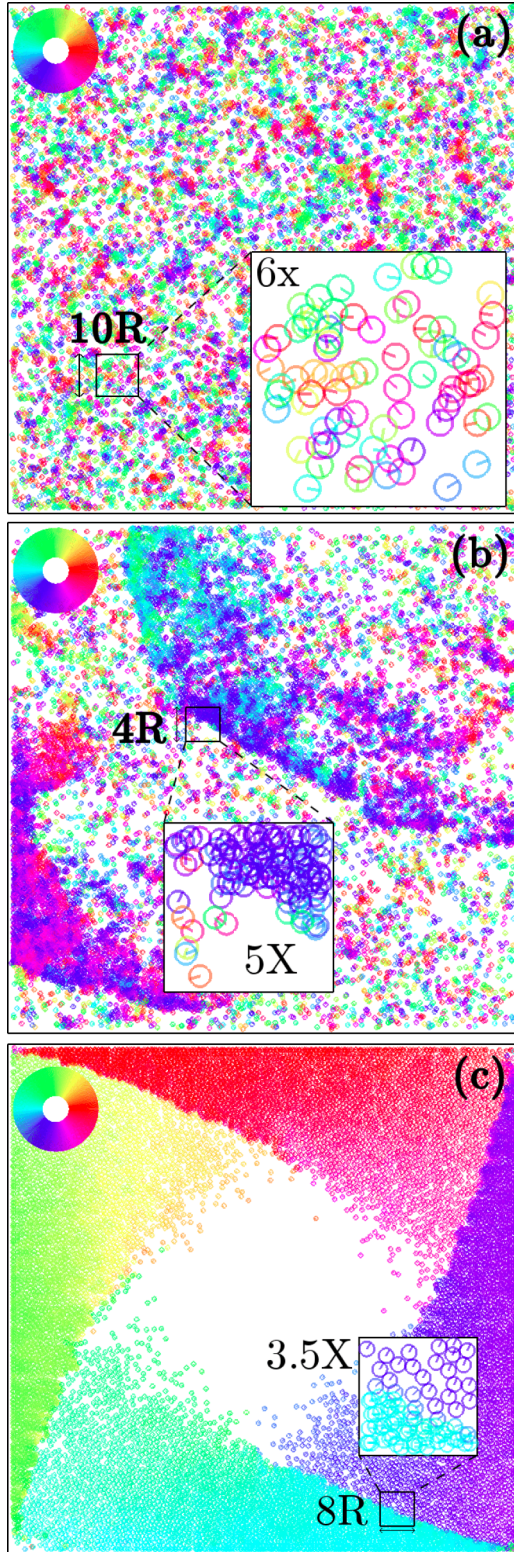
FIG. 6. Snapshots of the simulations with various noises and fixed repulsion factor $\alpha = 0.5$, initial density $\rho_0 = 1$, box size $L = 120R$, and noise intensity $\epsilon = 1.2, 0.8$, and 0 for (a), (b), and (c), respectively. Open circles indicate particles, and line segments inside circles are along the particle trajectories. Color (gray scale) shows the direction of motion corresponding to the color (gray scale) wheel located in the top-left corner of each box. Squared windows represent zooming in a part of the box; the length of the selected area and the magnification factor are written close to the corresponding window.

clumps in a square and circular box is square and circular, respectively. For negative α's, particles rotate toward each other, and if this attraction is small we see multiple clusters traveling and bouncing off the walls [Fig. 7(c)]. These clusters are extremely packed and unstable. They may divide into smaller groups or join together to make a bigger mass of particles. The division takes place when particles are more distant than their interaction range so that they cannot return to each other. Finally, a strong attraction produces vibrating rings of particles when they cannot escape from the ring [Fig. 7(d)].

To identify the detailed properties of these regimes, we look at velocity autocorrelations over time $[C_v(\tau) = (1/v_0^2)\langle \vec{v}_i(t) \cdot \vec{v}_i(t + \tau)\rangle_{i,t}]$ and space $[C_v(r) = (1/v_0^2)\langle \vec{v}_i(t) \cdot \vec{v}_j(t)\rangle_{i,j|r_{ij}=r}]$. We see that autocorrelations in time oscillate in both the vortex phase and the band structures (Fig. 8). The oscillation in the vortex phase [Fig. 8(a)], however, damps over time gradually. This damping is due to the different frequencies of rotation of the particles, and we demonstrate this fact in Appendix D. In contrast to the vortex phase, the traveling band-structure regime shows more robust $C_v(\tau)$ oscillations [Fig. 8(b)]. In this state, band structures travel in the medium with a constant speed that depends on the noise strength. These waves bounce from the walls and periodically move from one corner to another. Finally, in the homogeneous gaseous state, $C_v(\tau)$ spontaneously reaches zero [Fig. 8(b) $\epsilon = 1.2$].

In the vortex phase, $C_v(r)$ (Fig. 9) exhibits the behavior and characteristic length scale of rotation [Fig. 9(a)]. This length scale is the same as the box dimension. In higher noise, no negative correlation at long-range distances is seen except for the rotating pattern in $\epsilon = 0.6$ [Fig. 9(b)].

We plot $2M/Lv_0$ as a function of scaled noise ϵ/ϵ_c in Fig. 10. Figure 10 shows that M has a crossover behavior close to ϵ_c. Because $M \neq 0$ needs symmetry breaking, it seems that we have a phase transition from the disordered to the vortex phase near ϵ_c. Moreover, the closeness of this crossover to ϵ_c for different densities in Fig. 10 shows that the vortex phase is a consequence of the confinement of the polar state. However, a massive finite-size analysis is required to prove these facts.

To illustrate the different behaviors of the system and their regions in parameter space, we plot the map of parameters in Fig. 11. To construct different regions of the map, we do the following: We look at the angular momentum per particle $(2\langle M\rangle/Lv_0 > 0.5)$ to map points to the rotation phase. To recognize vibrating rings and disordered phases from moving clumps and clusters, we compute the local cohesion,

$$\Phi = \frac{1}{N_w}\left|\sum_{ij}\cos(\theta_i - \theta_j)\right|. \tag{19}$$

Here, N_w is the number of particles in a certain window, and the sum is over particles within that window.

By decreasing the noise, one can see (a) the homogeneous phase, (b) the inhomogeneous phase with curved stripes, and (c) the vortex phase. In the vortex phase, suppressed spreading and four defect lines are observable.
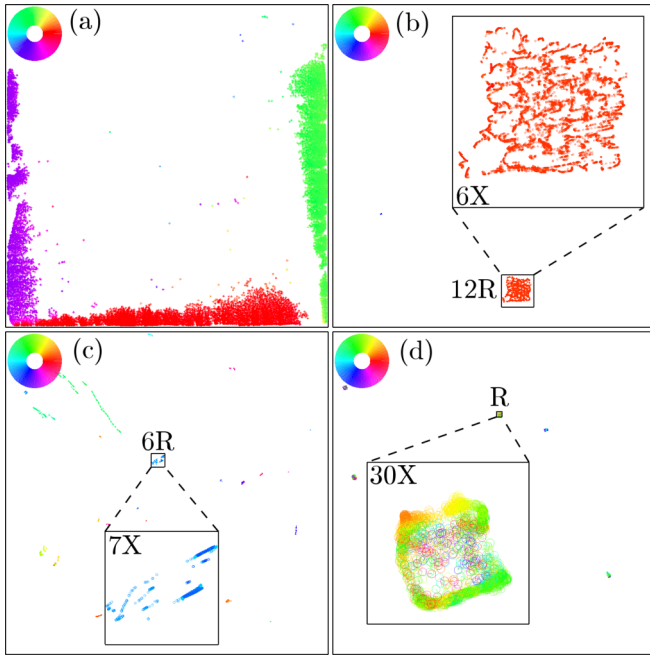
FIG. 7. Snapshots of the simulated system with $\rho_0 = 1$, $L = 120R$, $\epsilon = 0.1$, and different values of α. Open circles indicate particles, and line segments inside circles along the particle trajectories. Color (gray scale) shows the direction of motion corresponding to the color (gray scale) wheel located in the top-left corner of each box. Squared windows represent zooming in a part of the box; the length of the selected area and the magnification factor are written close to the corresponding window. (a) $\alpha = 0.01$, particles rotate cohesively close to the walls and a very small defect line is observable. (b) $\alpha = 0$, a clump forms with a large number of particles in a small area. This clump is moving and gets reflected from the walls; sometimes it is divided into smaller clumps due to the noise, and at other times small clumps join to make a bigger clump. (c) $\alpha = -0.01$, clusters of particles continuously divide and join during simulation. (d) $\alpha = -0.2$, vibrating rings emerge.

C. Suppressed spreading and defect lines

Suppressed spreading and the presence of defect lines are two of the interesting features of the system. For a clearer
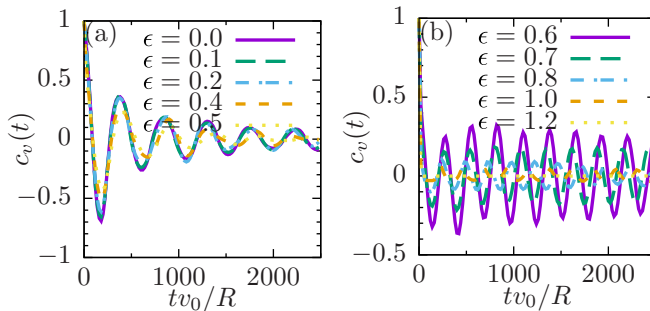

FIG. 8. Velocity autocorrelation over time for systems with $\rho_0 = 1$, $L = 120R$, $\alpha = 0.5$, and various ϵ. (a) The noise is lower than critical noise and the system is in the vortex phase. (b) A big polar rotating structure ($\epsilon = 0.6$), locally propagating band structures ($\epsilon = 0.7, 0.8,$ and 1.0), and the homogeneous gaseous phase ($\epsilon = 1.2$).
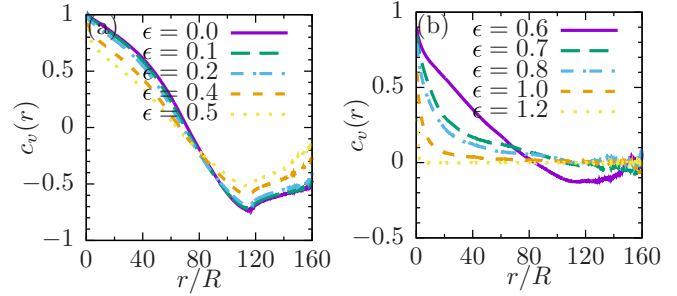

FIG. 9. Velocity autocorrelation over distance for systems with $\rho_0 = 1$, $L = 120R$, $\alpha = 0.5$, and various ϵ. (a) The noise is lower than critical noise and the system is in the vortex phase. (b) A big polar rotating structure ($\epsilon = 0.6$), locally propagating band structures ($\epsilon = 0.7, 0.8,$ and 1.0), and the homogeneous gaseous phase ($\epsilon = 1.2$).

observation of defect lines, we can measure the cohesion between particles. Figure 12 shows time-averaged $\rho(\vec{r})$, $\Phi(\vec{r})$, and $\vec{v}(\vec{r})$. Near the corners, the density reaches its highest value. The velocity field shows an outgoing flow of particles at each corner that is suppressed by the collision of incoming flow to the same corner. This collision creates a defect line that corresponds to lower cohesion but high density. The term "defect line" is used due to the spontaneous change of velocity at the boundary between incoming and outgoing flows.

Defect lines are also present in the solution of the continuum model introduced in Sec. III C. Density and velocity fields in the numerical solution and particle simulations are plotted in Figs. 13 and 14, respectively, for a system with $\rho_0 = 1$, $g_p = 2$, $\alpha = 0.5$, and $v_0 = 0.3$, which show excellent qualitative but not precise quantitative agreement between the simulation and the continuum model.

Figure 15 shows the change in the average density, cohesion, velocity, and rotational frequency of particles across a horizontal line $y = y_0$ for $y_0 = 53$ and $y_0 = 0$. One can see that
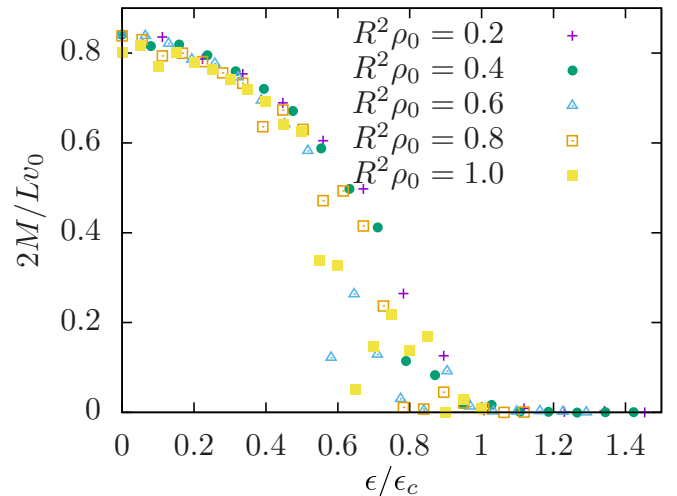

FIG. 10. Scaled angular momentum per particle ($2M/Lv_0$) vs scaled noise ϵ/ϵ_c for different values of density ρ_0. Simulation parameters are $\alpha = 0.5$ and $L = 120R$. Upon decreasing the noise, the system exhibits a behavior change. Moreover, the behavior change in different densities happens close to the same point.
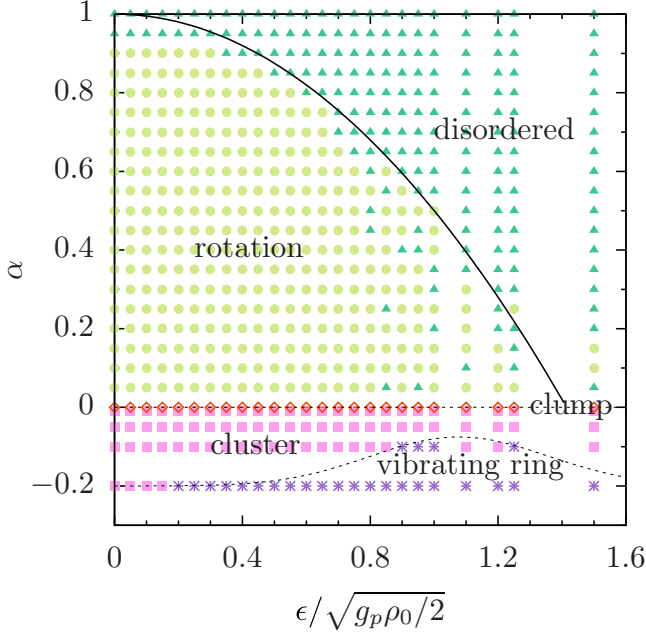
FIG. 11. Map of parameter space of the system with $\rho_0 = 1$ and $L = 60R$. This diagram is constructed from the results of 625 points, each averaged over 15 realizations. The dashed curves represent the boundary between regions with different behavior. The solid curve between rotation and the disordered phase is from the theoretical prediction of the nonpolar-to-polar transition. Each regime is recognized by looking at angular momentum and cohesion. Rotation is recognized by looking at the scaled angular momentum per particle ($2M/Lv_0$) greater than 0.5. Vibrating rings were recognized by local cohesion smaller than 0.1 when $\alpha < 0$. The remaining points are either in the moving clusters or the clumps regime. All points with $\alpha = 0$ correspond to the formation of moving clumps, and the rest of the points are in the moving clusters regime.

right after the defect (lower cohesion), the density decreases exponentially [Fig. 15(a)]. In examining the velocities, we find that they are tangent to the wall, and by moving away from the wall we see that the component of velocity perpendicular to the wall is independent of the horizontal position [Fig. 15(b)], and it is proportional to the distance from the wall [Fig. 15(d)]. This proportionality corresponds to the exponential shape of the defect line. To show this, we first define $u(x)$, the distance between the top defect line in Fig. 12(c) from the top wall as a function of x. The linear relation of the component of velocity perpendicular to the wall gives us $v_y = c_v u$, where c_v is a positive number. This linear relation enables us to find a differential equation with an exponential solution:

$$\frac{du(x)}{dx} = -\frac{v_y}{v_x} = -\frac{v_y}{\sqrt{1 - v_y^2}} \approx -v_y = c_v u(x). \quad (20)$$

Here we assume $|v_y| \ll 1$, which is clear from Fig. 15(d).

The defect lines in the experiment of Ref. [31] also seem to have an exponential form. We extracted experimental images from a movie in the supplemental material on the Quincke rotors experiment [31], and we assumed that the averaged gray
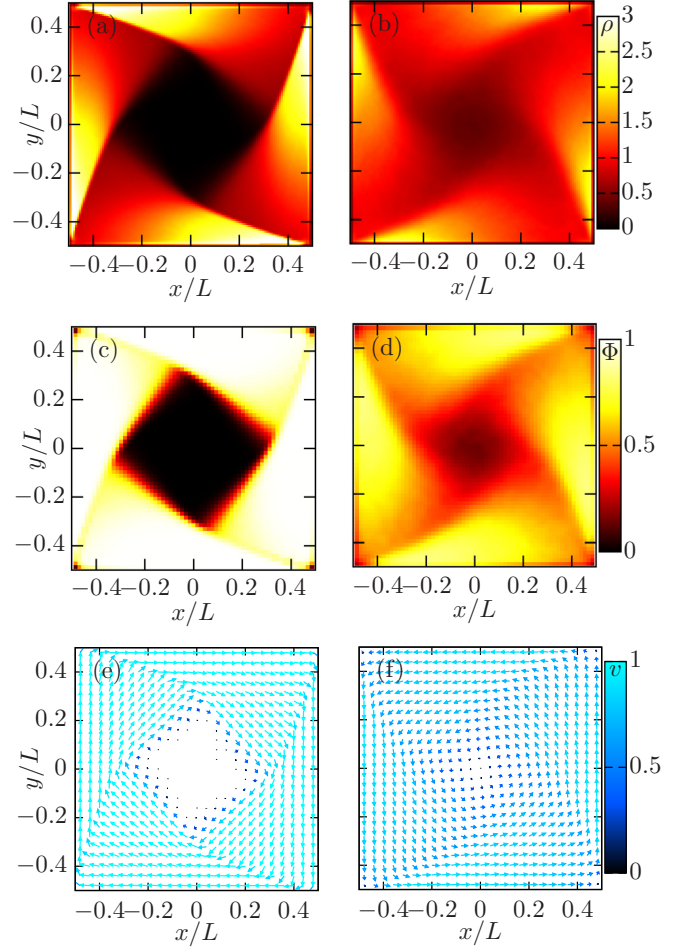

FIG. 12. Time average of ρ, Φ, and $\vec{v}$ in space for $\rho_0 = 1$ and $\epsilon = 0, 0.5$ in a box of size $L = 120R$. (a) and (b) Density with grid dimension 128 by 128. (c) and (d) Cohesion with grid dimension 64 by 64. (e) and (f) Velocity with grid dimension 25 by 25. Color (gray scale) corresponds to the magnitude of each field, and the lengths of the arrows in (e) and (f) show the average speed. Parts (a), (c), and (e) belong to the same noiseless simulation of a clockwise vortex ($\epsilon = 0$). Parts (b), (d), and (f) belong to the simulation of a counterclockwise vortex with noise ($\epsilon = 0.5$). Defect lines corresponding to suppressed spreading are observed in regions with low cohesion and high density.

scale over the images is proportional to the density. The forms of the defect lines in the simulation, the continuum model, and the experiment are sketched in Fig. 16, which shows a very good agreement between these three data sets.

Figure 15(c) shows that the angular velocity of particles across $y = 0$ is not constant. We also computed the average angular velocity ($\omega = \Delta\theta/\Delta t$) of any particle around the center of the box, and we observed that the angular velocity is almost proportional to the inverse of the distance from the center ($\omega \sim 1/r$). This means that the particles' velocity component perpendicular to their position vector is rather constant ($\omega = v_\perp/r$). The result shows that in the low-noise regime, $v_\perp \approx \langle v \rangle \approx v_0$. However, a reduction in $v_\perp$ as well as the time-averaged velocity of the particles is observed when the noise is high.
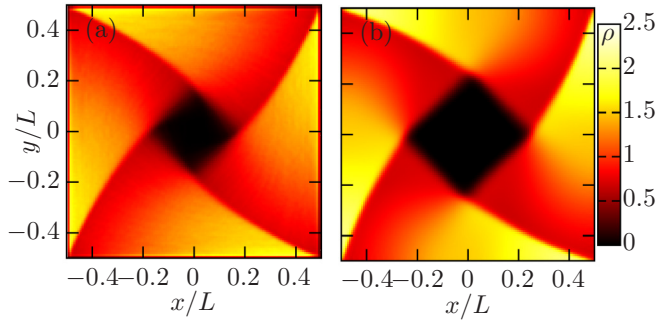
FIG. 13. Comparison of the averaged density field for (a) the particle model and (b) the continuum model. Parameters are set to $\rho_0 = 1$, $v_0 = 0.3$, $\alpha = 0.5$, $\epsilon = 0$, and $L = 120R$. The color (gray scale) represents density. The grid size is 128 by 128. A few points of the continuum model are in the range $\rho \in (-0.1, 0)$, but in order to obtain a better comparison we plot both maps in the same interval, $\rho \in (0, 2.5)$.

V. DISCUSSION

In this study, we presented a minimal model to mimic the behavior of Quincke rotors in a square box. In our model there is alignment and repulsion between particles. The model shows six different regimes by changing the noise strength and the ratio of alignment to repulsion. The observed regimes are homogeneous disordered, moving clumps, moving clusters, vibrating rings, traveling stripes, and a vortex state. Our focus in this paper was on the formation of a vortex. Vortex formation is a consequence of the confinement of a polar state. Actually, there is a crossover for the angular momentum of particles close to the transition point of a nonpolar to polar state. Further investigations with finite-size analysis could be done to accurately characterize the phase transition. In the vortex phase, defect lines are observed at the points where the particles suddenly change direction. As in the experiment, the defect lines in a vortex phase have fourfold symmetry, and each has an exponential form. This fourfold symmetry is because the spread of particle flow going out of a corner is suppressed by the collision of another flow, and a
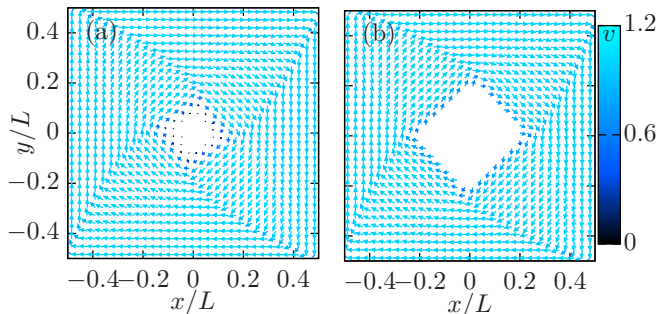

FIG. 14. Comparison of the averaged velocity field for (a) the particle model and (b) the continuum model. Parameters are set to $\rho_0 = 1$, $v_0 = 0.3$, $\alpha = 0.5$, $\epsilon = 0$, and $L = 120R$. The color (gray scale) represents the velocity magnitude. The length of the arrows is proportional to the speed. The grid size is 32 by 32. To enhance the velocity map of the continuum model, we removed points with density lower than 0.03 that have large computational errors.
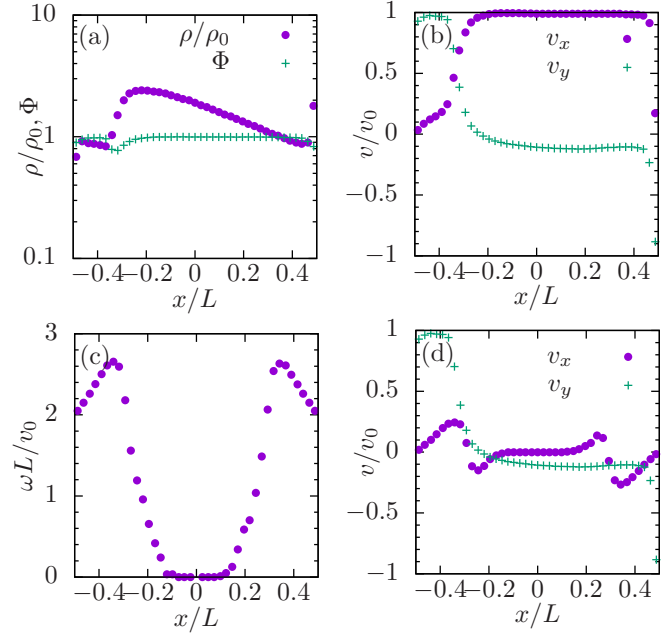

FIG. 15. Cross-sectional value of time-averaged fields. (a) ρ and Φ across the horizontal line $y = 53$. (b) and (d) Velocity components across horizontal lines for (b) $y = 53$ and (d) $y = 0$. (c) Angular velocity ω across the horizontal line $y = 0$. Simulation parameters are $\rho_0 = 1.0$, $\epsilon = 0.05$, and $L = 120R$. One can see that the density decreases exponentially and the cohesion has a falloff corresponding to crossing the defect line in (a). The velocity component perpendicular to the wall is constant along the wall (b), and it increases linearly with the distance from the wall (d). Finally, (c) shows that the rotation frequency of the particles depends on their position.

defect line emerges for each corner. The exponential form of the defect lines is also seen in experiment and our theory.

We derived hydrodynamic equations to describe the behavior of the system analytically. The usual method of deriving hydrodynamic equations gives us equations that can only predict the transition point, and they are not stable for the enumeration of the vortex phase. To enumerate the vortex phase, a more stable set of low-noise hydrodynamic equations is required. We introduced a method called "small deviation" to obtain stable equations. In this method, we assumed that in low noise, the distribution of the particle orientation is narrow. We did not assume any specific distribution (such as Gaussian or Poisson distribution), and we only assumed that the standard deviation and the higher cumulant of the distribution are small. Using the hydrodynamic equation of the small deviation approximation, we were able to describe our system theoretically in a vortex phase. The result of the theory is in very good agreement with simulation results. For example, we observed that in experiments, theory, and also simulations, the center of the box is empty. To test the theory further, we derived an analytic result for the density profile of a vortex in a circular box that exactly matches the result of the simulations. Therefore, the small deviation accurately describes our system in low noise. This small deviation could be used in the future as a helpful tool to study systems of active matter in low noise.
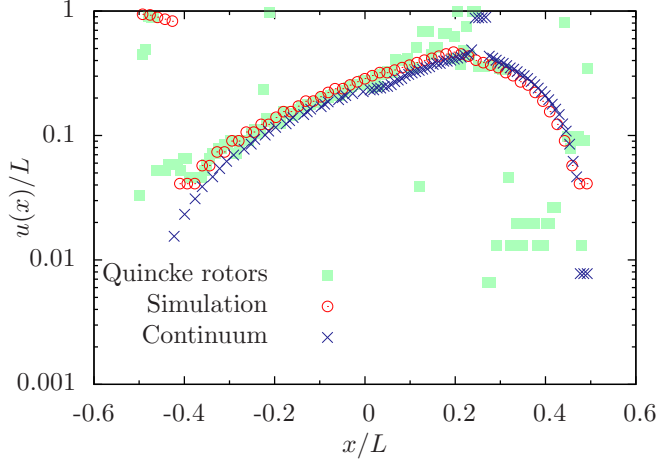
FIG. 16. The defect line distance from the wall u as a function of horizontal position x from the corner in three cases of Quincke rotors experiment, simulation, and continuum theory. Simulation and continuum parameters are set to $\rho_0 = 1$, $\alpha = 0.5$, $v_0 = 0.3$, $\epsilon = 0$, and $L = 120R$. Experimental data are averaged movie frames of Ref. [31] with an enhancement of the final image to avoid computational error. The gray scale of each point is proportional to the density. u is defined as the points where $|\frac{1}{\rho}\frac{\partial \rho}{\partial y}|_{[x, L/2-u(x)]} > 0.1$. One can see that at the interval $-0.3 < x/L < 0.2$ the defect line shape is exponential, which is in agreement with the exponential decay of density in Fig. 15(a). We also see that experiment, simulation, and the continuum model are all in good agreement.

As we mentioned, there is an empty region in the center of the box. Our theoretical and simulation results show that the size of this empty region depends on the strength of the repulsion, the density of the particles, and their speed. The speed dependence of the density profile could be used as a separator of fast- and slow-moving particles. Because the speed of Quincke rotors depends on their radius and other environmental factors [31], they are particularly good candidates for future experiments on this separation technique. Our next research goal is to study the behavior of mixtures of fast and slow particles using simulations. Other studies are also possible, such as a more precise study of the transition with finite-size scaling, or a study of confinement in other geometries, e.g., n-sided polygons. One could also find the

limit of n in an n-sided polygon in which the vortex no longer has the symmetry of the polygon. Finally, one can construct hydrodynamic equations using the Gaussian approximation, checking the accuracy of the results and comparing them with the results from the small deviation method [51].

APPENDIX A: HIGH-NOISE LIMIT

We use the Boltzmann approximation to derive the Fokker-Planck equation. Using the method presented in Ref. [52], we derive the Fokker-Planck equation for $f(\theta, \vec{r})$ up to second order of spatial derivatives [Eq. (10)]. The resulting drift velocity is

$$
\begin{aligned}
V_{\text{drift}} = (1 - \alpha) g_p \\
\times \left[\int_0^{2\pi} \sin(\theta' - \theta) \left(f(\theta', \vec{r}) + \frac{\nabla^2 f(\theta', \vec{r})}{8} \right) d\theta' \right] \\
+ \left[\frac{\alpha g_p}{3} \vec{\nabla} \rho(\vec{r}) \cdot (\hat{v}_\theta \wedge \hat{e}_z) \right],
\end{aligned} \tag{A1}
$$

where the first bracketed term is the alignment interaction and the second is the repulsion.

To construct the hydrodynamic equation from Eq. (10), we write the orientational density f in terms of Fourier components: $f(\theta, \vec{r}) = \frac{1}{2\pi} \sum_k e^{\iota k \theta} \tilde{f}_k$, where ι is an imaginary number, k is an integer number between $-\infty$ and $+\infty$, and $\tilde{f}_k$ is the kth Fourier component of f. Thanks to the linear independence of the Fourier basis $e^{\iota k \theta}$, we can split Eq. (10) into an infinite set of separate recurrence equations for different k in Fourier space with

$$
\begin{aligned}
\frac{\partial \tilde{f}_k(\vec{r})}{\partial t} = -D_r k^2 \tilde{f}_k + \frac{(1 - \alpha) g_p k}{2} \left[\tilde{f}_{k-1} \left(\tilde{f}_1 + \frac{1}{8} \nabla^2 \tilde{f}_1 \right) - \tilde{f}_{k+1} \left(\tilde{f}_{-1} + \frac{1}{8} \nabla^2 \tilde{f}_{-1} \right) \right] \\
- \frac{\alpha g_p k}{6} \vec{\nabla} \rho \cdot (\hat{x}(\tilde{f}_{k-1} - \tilde{f}_{k+1}) - \iota \hat{y}(\tilde{f}_{k-1} + \tilde{f}_{k+1})) - v_0 \partial_x \frac{\tilde{f}_{k-1} + \tilde{f}_{k+1}}{2} - v_0 \partial_y \frac{\tilde{f}_{k-1} - \tilde{f}_{k+1}}{2\iota}.
\end{aligned} \tag{A2}
$$

To deal with the equations, we need to find a closure. If we look at Eq. (A2), we see that there is a damping term $-D_r k^2 \tilde{f}_k$ with a time scale $\tau_k = -D_r k^2$, meaning that higher moments of $\tilde{f}_k$ vanish faster. Here we assume that moments of $\tilde{f}_k$ for $k \geqslant 3$ are zero and the second moments converge to their equilibrium values fast enough so that we can assume $\dot{\tilde{f}}_{\pm 2} = 0$. This assumption is valid until the damping terms for higher moments are dominant. Comparing the coefficients of

the RHS of Eq. (A2) when $k = 3$ with τ_3^{-1}, we obtain the conditions $D_r \gg \frac{(1-\alpha) g_p}{6}$, $D_r \gg \frac{\alpha g_p}{18}$, and $D_r \gg \frac{v_0}{9}$ to truncate Eq. (A2) for $k \geqslant 3$. Given the values of $\alpha = 0.5$, $g_p = 2$, and $v_0 = 1$ (the same as the simulations), we find the inequality $D_r \gg 0.16$, which satisfies all the conditions.

After the truncation, we can find $\tilde{f}_{\pm 2}$ in terms of $\tilde{f}_{\pm 1}$ and $\tilde{f}_0$. Then in the equation of $\tilde{f}_{\pm 1}$ we replace $\tilde{f}_{\pm 2}$ with $\tilde{f}_{\pm 1}$ and

$\tilde{f}_0$. Also, we use the facts that $\tilde{f}_0 = \rho$ [Eq. (6)] and $\tilde{f}_{\pm 1} = W_x \mp \iota W_y$ [Eq. (9)]. Then, with a straightforward calculation, we can solve separately for real and imaginary parts to find the hydrodynamic equations (11) and (12) with $\vec{W}_\nabla$ as

$$\vec{W}_\nabla = -\frac{\alpha^2 g_p^2}{72 D_r}|\vec{\nabla}\rho|^2 \vec{W} + \left[\left(\frac{v_0^2}{16 D_r} + \frac{(1-\alpha)\rho g_p}{16} \right)\nabla^2 \vec{W} - \frac{(1-\alpha)^2 g_p^2}{32 D_r}(\vec{W}\cdot\nabla^2\vec{W})\vec{W} \right] - \frac{(1-\alpha)g_p v_0}{16 D_r}\left[-\frac{5}{2}\vec{\nabla}W^2 \right.$$

$$+ 5\vec{W}\vec{\nabla}\cdot\vec{W} + 3\vec{W}\cdot\vec{\nabla}\vec{W} \Bigg] - \left(\frac{\alpha g_p}{6}\rho + \frac{v_0}{2} \right)\vec{\nabla}\rho + \frac{\alpha(1-\alpha)g_p^2}{12 D_r}(\vec{W}\cdot\vec{\nabla}\rho)\vec{W} + \frac{\alpha g_p v_0}{48 D_r}(2\vec{W}\nabla^2\rho + 2\vec{\nabla}\rho\cdot\vec{\nabla}\vec{W}$$

$$- 3\vec{\nabla}\cdot\vec{W}\vec{\nabla}\rho + 3\vec{\nabla}\rho \wedge (\vec{\nabla}\wedge\vec{W})). \tag{A3}$$

On the RHS of Eq. (A3), the first term introduces a reduction in polarity due to the net repulsive torque in the density gradient. The first bracketed term is very important for the spread of polarization. It is a diffusionlike term for $\vec{W}$ and comes from the alignment of neighboring particles. The second bracketed term comes from alignment interaction between particles, and it is well known in both phenomenological and analytical studies [16,41–43]. The rest of the equation shows an escape of particles from higher densities due to repulsion and advection.

APPENDIX B: LOW-NOISE LIMIT

Equation (10) is an equation for the dynamics of f. However, in our derivation it is more convenient to work with P instead of f. To find the evolution of P, we replace ρP with f in Eq. (10), and we also use the continuity equation [Eq. (11)] and Eq. (9) to replace $\dot{\rho}$ with $-v_0\vec{\nabla}\cdot\rho\langle\hat{v}_\theta\rangle$. Using simple calculations we find $\dot{P}$,

$$\frac{\partial P(\theta,\vec{r})}{\partial t} = -(1-\alpha)g_p\partial_\theta\left[P(\theta,\vec{r})\int_0^{2\pi}\sin(\theta'-\theta)\left(\rho P(\theta',\vec{r}) + \frac{\nabla^2\rho P(\theta',\vec{r})}{8} \right)d\theta' \right]$$

$$- \partial_\theta\left[\frac{\alpha g_p}{3}P(\theta,\vec{r})\vec{\nabla}\rho\cdot(\hat{v}_\theta\wedge\hat{e}_z) \right] + D_r\frac{\partial^2 P(\theta,\vec{r})}{\partial\theta^2} - \frac{v_0\hat{v}_\theta}{\rho}\cdot\vec{\nabla}[\rho P(\theta,\vec{r})] + \frac{v_0}{\rho}P(\vec{r},\theta)\vec{\nabla}\cdot[\rho\langle\hat{v}_\theta\rangle]. \tag{B1}$$

In our derivation, we need to find the evolution of many average fields over θ in space, such as $\langle\theta\rangle(\vec{r},t)$, $\langle\theta^2\rangle(\vec{r},t)$, and $\langle\hat{v}_\theta\rangle(\vec{r},t)$. Therefore, to simplify the calculation we define an arbitrary function $b(\theta)$ that could be θ, θ^2, and components of $\hat{v}_\theta$, and we find the governing dynamics of $\langle b(\theta)\rangle(\vec{r},t)$. Toward that end, we multiply both sides of Eq. (B1) with $b(\theta)$ and integrate both sides over θ from 0 to 2π,

$$\frac{d\langle b(\theta)\rangle}{dt} = (1-\alpha)g_p\langle b'(\theta)\sin(\theta'-\theta)\rangle_{\theta',\theta}\left(\rho + \frac{1}{8}\nabla^2\rho \right)$$

$$+ \frac{1}{8}(1-\alpha)g_p\rho(\vec{r})\langle b'(\theta)\nabla^2\langle\sin(\theta'-\theta)\rangle_{\theta'}\rangle_\theta + \frac{\alpha g_p}{3}\vec{\nabla}\rho(\vec{r})\cdot[\langle b'(\theta)\hat{v}_\theta\rangle\wedge\hat{e}_z] - \frac{v_0}{\rho}\vec{\nabla}\cdot[\rho(\vec{r})\langle b(\theta)\hat{v}_\theta\rangle]$$

$$+ \frac{1}{4}(1-\alpha)g_p\vec{\nabla}\rho(\vec{r})\cdot\langle b'(\theta)\vec{\nabla}\langle\sin(\theta'-\theta)\rangle_{\theta'}\rangle_\theta + \frac{v_0}{\rho}\langle b(\theta)\rangle\vec{\nabla}\cdot[\rho(\vec{r})\langle\hat{v}_\theta\rangle] + D_r\langle b''(\theta)\rangle + O(\nabla^3). \tag{B2}$$

We write $\langle\rangle_\theta$ and $\langle\rangle'_\theta$ to recognize the averaging over θ and θ', respectively. Because the noise is low, we can assume that the orientational probability distribution of particles, $P(\theta,\vec{r})$, is sharply peaked around the mean value $\langle\theta\rangle_\theta(\vec{r},t)$. In other words, the variance of θ, $\sigma_\theta^2 = \langle\theta^2\rangle_\theta - \langle\theta\rangle_\theta^2$, is very small ($\sigma_\theta^2 \ll 1$). Thus we can approximate $\sin(\theta'-\theta)$ in the averaging process with $\theta'-\theta$ to find an analytical expression. If we neglect derivatives to find homogeneous equations, for $b(\theta) = \theta$ and $b(\theta) = \theta^2$, we can find the evolution of the deviation,

$$\frac{d\sigma_\theta^2}{dt} = D_r - (1-\alpha)g_p\rho_0\sigma_\theta^2, \tag{B3}$$

where D_r is acting here as a source of dispersion for θ, while the alignment interaction $(1-\alpha)g_p\rho$ reduces the dispersion. From this equation, we find that σ_θ^2 decays with a time scale $\tau_\sigma = 1/(1-\alpha)g_p\rho_0$ to its equilibrium value $\sigma_\theta^2 = D_r/(1-\alpha)g_p\rho$. Our assumption for the sharpness of the distribution function is true when $\sigma_\theta^2 \ll 1$, and this gives us a limit for the noise, $D_r \ll (1-\alpha)g_p\rho$. By expanding $e^{\iota\theta}$ up to second order around the mean value $\langle\theta\rangle$ and using the facts that $\langle e^{\pm\iota\theta}\rangle = \mathcal{P}_x \pm \iota\mathcal{P}_y$ and $e^{\pm\iota\langle\theta\rangle} = \frac{1}{\mathcal{P}}(\mathcal{P}_x + \pm\iota\mathcal{P}_y)$, we can find a relation between σ_θ^2 and polarization $\mathcal{P}$ as $\mathcal{P} = (1 - \sigma_\theta^2/2)$. The same assumption—small

deviation—in Eq. (B2) with $b(\theta) = e^{\iota\theta}$ helps us to find the dynamics of the polarization, $\vec{\mathcal{P}}(\vec{r},t)$ [Eq. (14)], with $\vec{\mathcal{P}}_\nabla$ defined as

$$
\begin{aligned}
\vec{\mathcal{P}}_\nabla &= \frac{(1-\alpha)g_p}{4}[(1-\mathcal{P})\vec{\mathcal{P}}\nabla^2\rho] + \frac{(1-\alpha)g_p\rho}{8}[(2\mathcal{P}-1)\nabla^2\vec{\mathcal{P}} - (4\mathcal{P}-3)\hat{\mathcal{P}}\hat{\mathcal{P}}\cdot\nabla^2\vec{\mathcal{P}}] \\
&\quad + \frac{(1-\alpha)g_p}{4}\left[(2\mathcal{P}-1)\vec{\nabla}\rho\cdot\vec{\nabla}\vec{\mathcal{P}} - \frac{4\mathcal{P}-3}{2\mathcal{P}^2}\vec{\mathcal{P}}\vec{\nabla}\rho\cdot\vec{\nabla}\mathcal{P}^2\right] + \frac{\alpha g_p}{3}[(1-2P)\vec{\nabla}\rho + (4P-3)\hat{\mathcal{P}}\cdot\vec{\nabla}\rho\hat{\mathcal{P}}] \\
&\quad + \frac{v_0}{\rho}[2\vec{\nabla}[\rho(\mathcal{P}-1)] + \hat{\mathcal{P}}\cdot\vec{\nabla}[\rho(\mathcal{P}-1)(\mathcal{P}-3)\hat{\mathcal{P}}] + (\mathcal{P}-1)(\mathcal{P}-3)\hat{\mathcal{P}}\vec{\nabla}\cdot\hat{\mathcal{P}} - \vec{\mathcal{P}}\cdot\vec{\nabla}\vec{\mathcal{P}}] + O(\nabla^3). \quad \text{(B4)}
\end{aligned}
$$

The first bracketed term on the RHS of Eq. (B4) is a driving term, the second spreads polarization because of interaction with neighboring particles, the third shows an alignment competition between high- and low-density regions, the fourth represents the repulsion of particles (moving against $\vec{\nabla}\rho$), and the last one shows advection.

APPENDIX C: DENSITY PROFILE IN A CIRCULAR BOX

We use Eq. (16) and we set $D_r = 0$ to find a simpler density equation in a circular box,

$$
\rho(r) = \frac{3v_0}{\alpha g_p}\ln\left(\frac{r}{r_0}\right). \quad \text{(C1)}
$$

We integrate both sides of Eq. (C1) over the surface of the box. One should be aware that Eq. (C1) is not physically valid for $r < r_0$ because it gives negative density values at these points. Therefore, our integral must be from r_0 up to R_{box}. This integral is

$$
\int_{r_0}^{R_{\text{box}}} 2\pi r\rho(r)dr = \int_{r_0}^{R_{\text{box}}} 2\pi r\frac{3v_0}{\alpha g_p}\ln\left(\frac{r}{r_0}\right)dr. \quad \text{(C2)}
$$

The left-hand side is the total number of particles, and it is equal to $\pi R_{\text{box}}^2\rho_0$. The right-hand side can be computed using integration by parts,

$$
\pi R_{\text{box}}^2\rho_0 = \frac{3\pi v_0}{\alpha g_p}\left[-R_{\text{box}}^2\ln\left(\frac{r_0}{R_{\text{box}}}\right) - \frac{R_{\text{box}}^2}{2} + \frac{r_0^2}{2}\right]. \quad \text{(C3)}
$$

Dividing both sides of Eq. (C3) by πR_{box}^2, one obtains Eq. (17).

APPENDIX D: TIME AUTOCORRELATION DAMPING IN A VORTEX PHASE

An ordered vortex inside a circular geometry, $C_v(\tau)$, could be computed by its definition,

$$
\begin{aligned}
&\langle\vec{v}_i(t)\cdot\vec{v}_i(t+\tau)\rangle_{i,t} \\
&= \frac{1}{NT}\int_0^T dt\int\vec{v}(\vec{r},t)\cdot\vec{v}(\vec{r}+\Delta\vec{r},t+\tau)\rho(\vec{r})d\vec{r}, \quad \text{(D1)}
\end{aligned}
$$

where N is the total number of particles, T is the duration of averaging, $\vec{v}(\vec{r},t)$ is the average velocity field at point $\vec{r}$ and time t, and $\Delta\vec{r}$ is the displacement of particles at point $\vec{r}$ and time t during time τ.

If we suppose that all particles are rotating with their velocity v_0 on an annulus between two circles with radii $r_{\min}$ and $r_{\max}$ in the box, then $\Delta\vec{r}$ is easily computed in polar coordinates. The radial component r remains unchanged, and the polar coordinate ϕ changes by $\Delta\phi = v_0\tau/r$. We also know that the velocity of the particle rotates by the same amount, thus the angle between the two velocities is $\Delta\phi$ and $\vec{v}(\vec{r},t)\cdot\vec{v}(\vec{r}+\Delta\vec{r},t+\tau) = v_0^2\cos(\Delta\phi)$, which is independent of time t. This independence of time helps us to drop the time averaging of Eq. (D1). Furthermore, we replace the dot product of velocities with $v_0^2\cos(v_0\tau/r)$ in Eq. (D1) and write the integral over the surface of the annulus as an integral over r with its corresponding Jacobian $2\pi r$. The final result is

$$
C_v(\tau) = \frac{1}{N}\int_{r_{\min}}^{r_{\max}} 2\pi r\rho(r)\cos\left(\frac{v_0\tau}{r}\right)dr. \quad \text{(D2)}
$$

This nice result shows us the damping of $C_v(\tau)$ for large τ. In the large values of τ, the cosine in the integrand of Eq. (D2) changes fast, and if $\rho(r)$ is a smooth and slowly changing function, the positive and negative parts of the integral in one oscillation cancel each other out. Hence, the integration gives us a negligible result when τ is large.

[1] D. Biro, D. J. T. Sumpter, J. Meade, and T. Guilford, From compromise to leadership in pigeon homing, Curr. Biol. **16**, 2123 (2006).

[2] M. Nagy, Z. Akos, D. Biro, and T. Vicsek, Hierarchical group dynamics in pigeon flocks, Nature (London) **464**, 890 (2010).

[3] M. Ballerini, N. Cabibbo, R. Candelier, A. Cavagna, E. Cisbani, I. Giardina, V. Lecomte, A. Orlandi, G. Parisi, A. Procaccini, M. Viale, and V. Zdravkovic, Interaction ruling animal collective behavior depends on topological rather than metric distance: Evidence from a field study, Proc. Natl. Acad. Sci. (USA) **105**, 1232 (2008).

[4] Ch. Becco, N. Vandewalle, J. Delcourt, and P. Poncin, Experimental evidences of a structural and dynamical transition in fish school, Physica A **367**, 487 (2006).

[5] N. C. Makris, P. Ratilal, D. T. Symonds, S. Jagannathan, S. Lee, and R. W. Nero, Fish population and behavior revealed by instantaneous continental shelf-scale imaging, Science **311**, 660 (2006).

[6] D. Helbing, I. Farkas, and T. Vicsek, Simulating dynamical features of escape panic, Nature (London) **407**, 487 (2000).

[7] F. J. Ndlec, T. Surrey, A. C. Maggs, and S. Leibler, Self-organization of microtubules and motors, Nature (London) **389**, 305 (1997).

[8] V. Schaller, C. Weber, C. Semmrich, E. Frey, and A. R. Bausch, Polar patterns of driven filaments, Nature (London) **467**, 73 (2010).

[9] A. Czirók, E. Ben-Jacob, I. Cohen, and T. Vicsek, Formation of complex bacterial colonies via self-generated vortices, Phys. Rev. E **54**, 1791 (1996).

[10] F. Peruani, J. Starruß, V. Jakovljevic, L. Søgaard-Andersen, A. Deutsch, and M. Bär, Collective Motion and Nonequilibrium Cluster Formation in Colonies of Gliding Bacteria, Phys. Rev. Lett. **108**, 098102 (2012).

[11] V. Narayan, S. Ramaswamy, and N. Menon, Long-lived giant number fluctuations in a swarming granular nematic, Science **317**, 105 (2007).

[12] J. Baker and A. Kudrolli, Maximum and minimum stable random packings of platonic solids, Phys. Rev. E **82**, 061304 (2010).

[13] T. Vicsek and A. Zafeiris, Collective motion, Phys. Rep. **517**, 71 (2012).

[14] M. C. Marchetti, J. F. Joanny, S. Ramaswamy, T. B. Liverpool, J. Prost, M. Rao, and R. Aditi, Hydrodynamics of soft active matter, Rev. Mod. Phys. **85**, 1143 (2013).

[15] T. Vicsek, A. Czirók, E. Ben-Jacob, I. Cohen, and O. Shochet, Novel Type of Phase Transition in a System of Self-Driven Particles, Phys. Rev. Lett. **75**, 1226 (1995).

[16] J. Toner and Y. Tu, Long-Range Order in a Two-Dimensional Dynamical xy Model: How Birds Fly Together, Phys. Rev. Lett. **75**, 4326 (1995).

[17] J. Toner and Y. Tu, Flocks, herds, and schools: A quantitative theory of flocking, Phys. Rev. E **58**, 4828 (1998).

[18] A. Baskaran and M. C. Marchetti, Hydrodynamics of self-propelled hard rods, Phys. Rev. E **77**, 011920 (2008).

[19] J. Tailleur and M. E. Cates, Statistical Mechanics of Interacting Run-and-Tumble Bacteria, Phys. Rev. Lett. **100**, 218103 (2008).

[20] F. D. C. Farrell, M. C. Marchetti, D. Marenduzzo, and J. Tailleur, Pattern Formation in Self-Propelled Particles with Density-Dependent Motility, Phys. Rev. Lett. **108**, 248101 (2012).

[21] N. Shimoyama, K. Sugawara, T. Mizuguchi, Y. Hayakawa, and M. Sano, Collective Motion in a System of Motile Elements, Phys. Rev. Lett. **76**, 3870 (1996).

[22] S. R. McCandlish, A. Baskaran, and M. F. Hagan, Spontaneous segregation of self-propelled particles with different motilities, Soft Matter **8**, 2527 (2012).

[23] H. Chaté, F. Ginelli, P. F. Grégoire, and F. Raynaud, Modeling collective motion: Variations on the Vicsek model, Europhys. J. B **64**, 451 (2008).

[24] P. Romanczuk and L. Schimansky-Geier, Brownian Motion with Active Fluctuations, Phys. Rev. Lett. **106**, 230601 (2011).

[25] P. Romanczuk and L. Schimansky-Geier, Mean-field theory of collective motion due to velocity alignment, Ecol. Complex. **10**, 83 (2012).

[26] A. P. Solon, Y. Fily, A. Baskaran, M. E. Cates, Y. Kafri, M. Kardar, and J. Tailleur, Pressure is not a state function for generic active fluids, Nat. Phys. **11**, 673 (2015).

[27] J. B. Caussin, A. Solon, A. Peshkov, H. Chaté, T. Dauxois, J. Tailleur, V. Vitelli, and D. Bartolo, Emergent Spatial Structures in Flocking Models: A Dynamical System Insight, Phys. Rev. Lett. **112**, 148102 (2014).

[28] A. Ordemann, G. Balazsi, and F. Moss, Pattern formation and stochastic motion of the zooplankton daphnia in a light field, Physica A **325**, 260 (2003).

[29] D. L. Blair, T. Neicu, and A. Kudrolli, Vortices in vibrated granular rods, Phys. Rev. E **67**, 031303 (2003).

[30] A. Kudrolli, G. Lumay, D. Volfson, and L. S. Tsimring, Swarming and Swirling in Self-Propelled Polar Granular Rods, Phys. Rev. Lett. **100**, 058001 (2008).

[31] A. Bricard, J. B. Caussin, N. Desreumaux, O. Dauchot, and D. Bartolo, Emergence of macroscopic directed motion in populations of motile colloids, Nature (London) **503**, 95 (2013).

[32] L. H. Cisneros, J. O. Kessler, S. Ganguly, and R. E. Goldstein, Dynamics of swimming bacteria: Transition to directional order at high concentration, Phys. Rev. E **83**, 061907 (2011).

[33] J. Dunkel, S. Heidenreich, K. Drescher, H. H. Wensink, M. Bär, and R. E. Goldstein, Fluid Dynamics of Bacterial Turbulence, Phys. Rev. Lett. **110**, 228102 (2013).

[34] M. R. D'Orsogna, Y. L. Chuang, A. L. Bertozzi, and L. S. Chayes, Self-Propelled Particles with Soft-Core Interactions: Patterns, Stability, and Collapse, Phys. Rev. Lett. **96**, 104302 (2006).

[35] Y. Sumino, K. H. Nagai, Y. Shitaka, D. Tanaka, K. Yoshikawa, H. Chaté, and K. Oiwa, Large-scale vortex lattice emerging from collectively moving microtubules, Nature (London) **483**, 448 (2012).

[36] R. Gromann, P. Romanczuk, M. Bär, and L. Schimansky-Geier, Vortex Arrays and Mesoscale Turbulence of Self-Propelled Particles, Phys. Rev. Lett. **113**, 258104 (2014).

[37] K. H. Nagai, Y. Sumino, R. Montagne, I. S. Aranson, and H. Chaté, Collective Motion of Self-Propelled Particles with Memory, Phys. Rev. Lett. **114**, 168001 (2015).

[38] Y. Limon Duparcmeur, H. Herrmann, and J. P. Troadec, Spontaneous formation of vortex in a system of self motorised particles, J. Phys. I **5**, 1119 (1995).

[39] D. Groman, I. S. Aranson, and E. Ben Jacob, Emergence of agent swarm migration and vortex formation through inelastic collisions, New J. Phys. **10**, 023036 (2008).

[40] A. Bricard, J. B. Caussin, D. Das, C. Savoie, V. Chikkadi, K. Shitara, O. Chepizhko, F. Peruani, D. Saintillan, and D. Bartolo, Emergent vortices in populations of colloidal rollers, Nat. Commun. **6**, 7470 (2015).

[41] E. Bertin, M. Droz, and G. Grégoire, Boltzmann and hydrodynamic description for self-propelled particles, Phys. Rev. E **74**, 022101 (2006).

[42] J. Toner, Y. Tu, and S. Ramaswamy, Hydrodynamics and phases of flocks, Ann. Phys. (N.Y.) **318**, 170 (2005).

[43] A. Baskaran and M. C. Marchetti, Enhanced Diffusion and Ordering of Self-Propelled Rods, Phys. Rev. Lett. **101**, 268101 (2008).

[44] H. Uecker, A short ad hoc introduction to spectral methods for parabolic PDE and the Navier–Stokes equations, in *Modern Computational Science*, Vol. 09, edited by R. Leidl and A. Hartmann (BIS Verlag, Oldenburg, 2009), pp. 169–212.

[45] C. Canuto, M. Y. Hussaini, A. M. Quarteroni, A. Thomas, and J. Zang, *Spectral Methods in Fluid Dynamics*, Scientific Computation (Springer, Berlin, 1993).

[46] A. Longtin, Stochastic dynamical systems, Scholarpedia **5**, 1619 (2010), revision 91828.

[47] G. Grégoire and H. Chaté, Onset of Collective and Cohesive Motion, Phys. Rev. Lett. **92**, 025702 (2004).

[48] H. Chaté, F. Ginelli, G. Grégoire, and F. Raynaud, Collective motion of self-propelled particles interacting without cohesion, Phys. Rev. E **77**, 046113 (2008).

[49] E. Bertin, M. Droz, and G. Grégoire, Hydrodynamic equations for self-propelled particles: Microscopic derivation and stability analysis, J. Phys. A **42**, 445001 (2009).

[50] See Supplemental Material at http://link.aps.org/supplemental/10.1103/PhysRevE.93.032113 for movies of the six different regimes observed during the simulations.

[51] B. Sonnenschein and L. Schimansky-Geier, Approximate solution to the stochastic Kuramoto model, Phys. Rev. E **88**, 052111 (2013).

[52] D. S. Dean, Langevin equation for the density of a system of interacting Langevin processes, J. Phys. A **29**, L613 (1996).